




Article

Eco-Friendly Anionic Surfactant for the Removal of Methyl Red from Aqueous Matrices

Yago N. Teixeira ¹, Jorge M. C. Menezes ¹, Raimundo N. P. Teixeira ², Francisco J. Paula Filho ¹
and Thiago M. B. F. Oliveira ^{1,*}

¹ Science and Technology Center, Federal University of Cariri, Av. Tenente Raimundo Rocha, 1639, Cidade Universitária, Juazeiro do Norte 63048-080, Brazil

² Biological Chemistry Department, Regional University of Cariri, Rua Coronel Antônio Luiz, 1161, Pimenta, Crato 63100-000, Brazil

* Correspondence: thiago.mielle@ufca.edu.br; Tel.: +55-88-3221-9564

Abstract: This study aimed to evaluate the methyl red (MR) removal efficiency from aqueous matrices using an eco-friendly anionic surfactant (a calcium surfactant, or CaSF), obtained from frying oil residue. Data obtained by infrared spectroscopy revealed several functional groups that favor the capture of the dye by chemisorption by forming hydrogen bonds and covalent interactions. The kinetic testing results fit the pseudo-second order model, reaching equilibrium in 30 min. Adsorption was greatly influenced by temperature. The Langmuir isotherm was the one best fitting the process at 20 °C, while the Dubinin–Radushkevich isotherm fitted it better at higher temperatures. Under optimized conditions, the maximal MR adsorption capacity of CaSF reached 53.59 mg·g⁻¹ (a removal rate of 95.15%), proving that the adsorbent at hand can be an excellent alternative for the removal of undesirable levels of MR present in aqueous matrices.

Keywords: anionic surfactant; adsorption; methyl red; azo dye removal



Citation: Teixeira, Y.N.; Menezes, J.M.C.; Teixeira, R.N.P.; Paula Filho, F.J.; Oliveira, T.M.B.F. Eco-Friendly Anionic Surfactant for the Removal of Methyl Red from Aqueous Matrices. *Textiles* **2023**, *3*, 52–65. <https://doi.org/10.3390/textiles3010005>

Academic Editors: Hafeezullah Memon and Narcisa Vrinceanu

Received: 10 December 2022

Revised: 31 December 2022

Accepted: 19 January 2023

Published: 28 January 2023



Copyright: © 2023 by the authors. Licensee MDPI, Basel, Switzerland. This article is an open access article distributed under the terms and conditions of the Creative Commons Attribution (CC BY) license (<https://creativecommons.org/licenses/by/4.0/>).

1. Introduction

Colored effluents from the textile, paint, paper and leather industries are among the main sources of water pollution and can drastically affect the biota and the natural aquatic balance. The presence of dyes in the water can affect photosynthesis even at low concentrations (<1 mg·L⁻¹), while many of them have a highly stable chemical structure, making their natural biodegradation difficult [1,2].

About 800,000 tons of synthetic dyes are produced annually and approximately half of that amount are azo dyes [3,4]. Azo dyes are resistant to traditional effluent treatment processes; they contribute to an increase in the total organic carbon content and turbidity, and aggravate the eutrophic processes taking place in the receiving water bodies. Furthermore, azo dyes pose a potential risk to public health, being associated with the occurrence of allergies, mutations and cancer even at trace levels [5,6]. Therefore, the removal of dyes from effluents before they are released into natural water bodies is critical.

Methyl red (MR, Figure 1) is an anionic azo dye, commonly used in the printing and dyeing industries due to its high color-fixing performance and mild fading [7]. Several techniques are used for the removal of this pollutant from effluents, among them are those based on the Fenton process [8], hydrogen peroxide-mediated oxidation [9], liquid–liquid extraction [10], anaerobic degradation [11], bacterial degradation [12,13] and adsorption [14]. Among these techniques, adsorption has gained significant notoriety due to its high efficiency and low cost. Several works have already studied the effectiveness of MR removal from water using different types of adsorbents, such as modified coconut shell [15], biochar [16], activated carbon [1], clay [17], chitosan [18], nanocomposites [19], eggshell [20], organosilicons [21] and sodium alginate flocs [22,23].

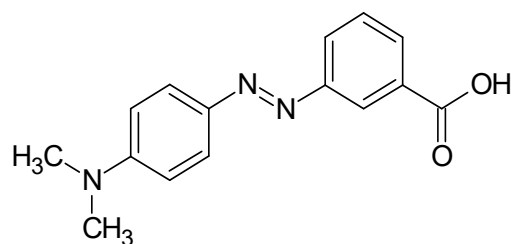


Figure 1. Structural formula of MR dye.

A calcium surfactant (CaSF) is an amphiphilic compound with a hydrophobic anionic chain that facilitates the interaction with organic compounds of a similar nature. Therefore, CaSF can sequester/adsorb dyes present in liquid effluents, thus reducing their pollutant load. The use of surfactants to remove benzene [24], phenol [25], dioxins [26], antioxidants [27], pesticides [28], heavy metals [29] and aniline [30] has also been studied. The use of anionic surfactants to remove dyes is a recent technology and needs further research to improve the technique and design future pilot projects. With that in mind, this study aimed to evaluate the efficiency of CaSF as a sequestering agent for MR in a synthetic effluent, contributing new alternatives for the sound management of liquid discharges containing undesirable levels of this azo dye. It is also worth noting that the proposed method is in line with the United Nations' Sustainable Development Goals, contributing new ideas for waste minimization and the use of sustainable materials, as frying oil waste is used as raw material for the production of the surfactant.

2. Materials and Methods

2.1. Chemicals

Frying oil residues (soybean oil, SB, and pork fat, PF) were collected from volunteers' homes in the city of Juazeiro do Norte, Brazil. Sodium hydroxide (NaOH), calcium chloride (CaCl₂), sodium chloride (NaCl) and MR dye (C₁₅H₁₅N₃O₂) were obtained from Synth, Diadema, Brazil. Hydrochloric acid (HCl) was purchased from Êxodo Científica, Sumaré, Brazil.

2.2. CaSF Synthesis

CaSF was produced through the saponification of frying residue, using NaOH. The percentage of SB and PF in the residue was 95 wt% and 5 wt%, respectively. The proportion of the different fatty acids present in SB/PF, together with their structural properties, is summarized in Table 1. Subsequently, 10 g of the anionic surfactant was dissolved in 1.60 L of deionized water under stirring at 100 rpm at 50 °C. After its complete dissolution, 0.40 L of a 0.065 M CaCl₂ solution was added, the heating was turned off and the stirring was reduced to 20 rpm for 10 min for the CaSF to form. The CaSF flocs were filtered and dried in a microwave oven for 5 min. After drying, the CaSF was macerated and sieved. CaSF granulometry was 40–50 mesh size. The generic structural formula of CaSF is represented in Figure 2.

Table 1. Percentage of fatty acids present in the SB/PF used to synthesize the anionic surfactant.

Fatty Acids (Carbon Atoms)	SB (wt%)	PF (wt%)	Type
Myristic (C14)	0.20	2.00	Saturated
Palmitic (C16)	11.35	27.00	Saturated
Stearic (C18)	4.15	11.00	Saturated
Palmitoleic (C16)	0.05	4.00	Unsaturated
Oleic (C18)	25.30	44.00	Unsaturated
Linoleic (C18)	50.75	11.00	Unsaturated
Linolenic (C18)	8.20	1.00	Unsaturated

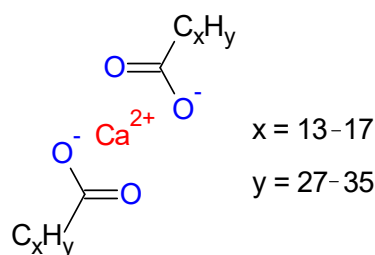


Figure 2. General representation of the CaSF structure.

2.3. CaSF Characterization

CaSF was analyzed by FTIR (PerkinElmer, Spectrum Two, Beaconsfield, United Kingdom) before and after MR adsorption in order to identify the surface functional groups responsible for dye capture. The analyzed spectra were in the range of $4000\text{--}450\text{ cm}^{-1}$ with a resolution of 4 cm^{-1} , using samples of the material dispersed in potassium bromide. To determine the point of zero charge (pH_{PZC}), eleven NaCl solutions (0.1 M, 20 mL) were prepared within an initial pH range of 1 to 11. The pH of the solutions was adjusted with the addition of 0.01 M HCl or NaOH. These solutions were transferred to Erlenmeyer flasks containing 20 mg of CaSF and subsequently stirred at 100 rpm for 6 h. The initial and final pH of the solutions were measured using a pH meter (Orion 5-Star probe, Thermo Scientific, Beverly, MA, USA). The [Initial pH—Final pH] was calculated and plotted vs. [Initial pH] to determine the pH_{PZC} . The point where [Initial pH—Final pH] crosses the origin was established as the pH_{PZC} [14].

2.4. Adsorption Experiments

A $100\text{ mg}\cdot\text{L}^{-1}$ stock solution of MR was prepared by dissolving the MR in deionized water with vigorous stirring. Samples with different concentrations were prepared from the stock solution. The adsorption experiments were carried out in batches, by stirring the CaSF together with buffered (acetate buffer) MR solutions. Soon after, CaSF was separated from the samples by filtration. The MR concentration in the samples, before and after adsorption, was determined using a UV spectrophotometer (Shimadzu, UV 1800, Kyoto, Japan) adjusted to 525 nm. The amount of dye adsorbed on the CaSF ($\text{mg}\cdot\text{g}^{-1}$) and the removal efficiency were calculated using Equations (1)–(3):

$$q_t = \left(\frac{C_o - C_t}{m} \right) V \quad (1)$$

$$q_e = \left(\frac{C_o - C_e}{m} \right) V \quad (2)$$

$$\% \text{ Removal efficiency} = \left(\frac{C_o - C_e}{C_o} \right) 100 \quad (3)$$

where C_o , C_t and C_e are the dye concentrations at the initial time, at a given time and at equilibrium, respectively ($\text{mg}\cdot\text{L}^{-1}$), q_t and q_e are the adsorption capacities at a given time and at equilibrium, respectively ($\text{mg}\cdot\text{g}^{-1}$), m is the mass of CaSF (g) and V is the volume of the solution (L).

2.5. Kinetics Studies

The surfactant's optimal dosage was evaluated using different CaSF concentrations (1, 2, 4, 5, 8 and $10\text{ g}\cdot\text{L}^{-1}$), which were mixed with $10\text{ mg}\cdot\text{L}^{-1}$ MR and stirred at 100 rpm for 30 min at $20\text{ }^\circ\text{C}$. The adsorption kinetics were assessed over 300 min under ideal conditions ($10\text{ g}\cdot\text{L}^{-1}$ CaSF, $\text{pH} = 4$, $20\text{ }^\circ\text{C}$, 100 rpm). The results were analyzed using the pseudo-

first order (PFO) (Equation (4)), pseudo-second order (PSO) (Equation (5)) and Elovich (Equation (6)) kinetic models [31,32].

$$q_t = q_e \left(1 - e^{-k_1 t}\right) \quad (4)$$

$$q_t = \frac{q_e^2 k_2 t}{1 + q_e k_2 t} \quad (5)$$

$$q_t = \frac{1}{\beta} \ln(1 + \alpha \beta t) \quad (6)$$

where k_1 and k_2 are the adsorption velocity constants of the PFO (min^{-1}) and PSO ($\text{g} \cdot \text{mg}^{-1} \cdot \text{min}^{-1}$), respectively, α is the initial adsorption rate ($\text{mg} \cdot \text{g}^{-1} \cdot \text{min}^{-1}$), β is the desorption constant ($\text{mg} \cdot \text{g}^{-1}$) and t is time (min).

2.6. Diffusion Mechanism

The adsorption mechanism was analyzed using the intraparticle diffusion (Weber–Morris) (Equation (7)) and the Boyd diffusion (Equation (8)) models [31].

$$q_t = k_{di} t^{1/2} + C \quad (7)$$

$$F = \frac{q_t}{q_e} \quad (8)$$

where k_{di} is the mass transfer coefficient ($\text{mg} \cdot \text{g}^{-1} \cdot \text{min}^{-1/2}$), C is the constant associated with the thickness of the boundary layer ($\text{mg} \cdot \text{g}^{-1}$) and F is the fraction of MR adsorbed at any given time. B_t (the mathematical function of F) can be calculated by Equations (9) and (10).

$$B_t = \left[\sqrt{\pi} - \sqrt{\pi - \left(\frac{\pi^2 F}{3}\right)} \right]^2 \text{ If } F < 0.85 \quad (9)$$

$$B_t = -0.4977 - \ln(1 - F) \text{ If } F > 0.85 \quad (10)$$

B_t was calculated for each value of F and then a $B_t \times F$ graph was plotted. The linear regression of the $B_t \times F$ graph provides the angular coefficient and the Boyd constant (B). The diffusion coefficient, D ($\text{cm}^2 \cdot \text{s}^{-1}$), can be calculated from B using Equation (11).

$$D = \frac{Bd^2}{60\pi^2} \quad (11)$$

where d is the mean diameter of the particles (cm).

2.7. Equilibrium Study

In the equilibrium study, samples containing concentrations of 5–100 $\text{mg} \cdot \text{L}^{-1}$ of MR at a total volume of 25 mL were treated under ideal conditions ($\text{CaSF} = 10 \text{ g} \cdot \text{L}^{-1}$, $\text{pH} = 4$, $t = 30 \text{ min}$, 100 rpm). The equilibrium results were analyzed using the Freundlich (Equation (12)), Langmuir (Equation (13)), Temkin (Equation (14)) and Dubinin–Radushkevich (DR) (Equation (15)) isotherms [31].

$$q_e = k_F C_e^{1/n} \quad (12)$$

$$q_e = \frac{q_{max} k_L C_e}{1 + k_L C_e} \quad (13)$$

$$q_e = \frac{RT}{b} \ln(k_T C_e) \quad (14)$$

$$q_e = q_m \exp \left\{ -k_{DR} \left[RT \ln \left(1 + \frac{1}{C_e} \right) \right]^2 \right\} \quad (15)$$

where k_F , k_L , k_T and k_{DR} are the constants of the Freundlich ($\text{mg}\cdot\text{g}^{-1}(\text{mg}\cdot\text{L}^{-1})$), Langmuir ($\text{L}\cdot\text{mg}^{-1}$), Temkin ($\text{L}\cdot\text{mg}^{-1}$) and DR ($\text{mol}^2\cdot\text{kJ}^{-2}$) isotherms, respectively, n is the constant related to the heterogeneity of the CaSF surface, q_{max} is the maximal adsorption capacity ($\text{mg}\cdot\text{g}^{-1}$), b is the constant related to the heat of adsorption ($\text{kJ}\cdot\text{mol}^{-1}$), R is the universal gas constant ($8.314\text{ J}\cdot\text{mol}^{-1}\cdot\text{K}^{-1}$), T is the process temperature (K) and q_m is the maximal adsorption capacity of the monolayer ($\text{mg}\cdot\text{g}^{-1}$).

The k_{DR} constant is associated with the mean adsorption energy (E), which can be calculated by Equation (16).

$$E = \frac{1}{\sqrt{2k_{DR}}} \quad (16)$$

The value of E provides information about the nature of the process, i.e., whether it is a physical adsorption ($E < 8\text{ kJ}\cdot\text{mol}^{-1}$), a ion exchange ($8 < E < 16\text{ kJ}\cdot\text{mol}^{-1}$) or a chemisorption ($E > 16\text{ kJ}\cdot\text{mol}^{-1}$) [32].

2.8. Statistical Error Analysis

Using the adjusted determination coefficient (R_{adj}^2) alone in order to adjust the experimental data to theoretical kinetics models and adsorption isotherms has its limitations and can lead to wrong conclusions. Therefore, other statistical error functions, such as the Chi-squared (X^2) test (Equation (17)) and the residual sum of squares (RSS) (Equation (18)), were used to validate the most appropriate kinetics and isothermal models. The corrected Akaike information criterion (AICc) (Equation (19)) was used for model comparison [31].

$$X^2 = \sum_{i=1}^z \frac{(q_{exp} - q_{calc})^2}{q_{exp}} \quad (17)$$

$$RSS = \sum_{i=1}^z (q_{exp} - q_{calc})^2 \quad (18)$$

$$AICc = z \ln\left(\frac{RSS}{z}\right) + 2k + \frac{2k(k-1)}{z-k-1} \quad (19)$$

where q_{exp} and q_{calc} are the experimental and model-calculated adsorption capacities, respectively, z is the number of experimental points and k is the number of parameters of the model.

3. Results and Discussion

3.1. CaSF Characterization

The main functional groups on the CaSF surface were analyzed by FTIR before and after MR adsorption (Figure 3). The FTIR spectra (Figure 3) showed several absorption peaks, indicating the presence of different functional groups at different wavenumbers, namely 3417 cm^{-1} , associated with the elongation of the OH^- functional group, which indicates the presence of hydrogen bonds; 3011 cm^{-1} , typical of simple unsaturated olefinic compounds ($\text{CH}=\text{CH}$); and $2921\text{--}2850\text{ cm}^{-1}$, corresponding to the C-H stretch in long-chain linear aliphatic compounds. The good resolution and high intensity of these peaks also suggest that CaSF does not have impurities in its molecular structure [33,34].

The peak at 1693 cm^{-1} indicates alkenyl stretching ($\text{CH}=\text{CH}$). The sequences of peaks at $1578\text{--}1541\text{ cm}^{-1}$ and $1432\text{--}1420\text{ cm}^{-1}$ suggest the presence of a carboxylic acid salt (COO^-). The peak at 1113 cm^{-1} indicates the presence of saturated esters (COO). Finally, the peaks at $722\text{--}675\text{ cm}^{-1}$ indicate out-of-plane olefin deformations ($\text{CH}=\text{CH}$). Most functional groups were affected after CaSF came into contact with the dye. The disappearance of certain bands and the reduction in the intensity of some peaks point to the occurrence of MR adsorption on the CaSF surface.

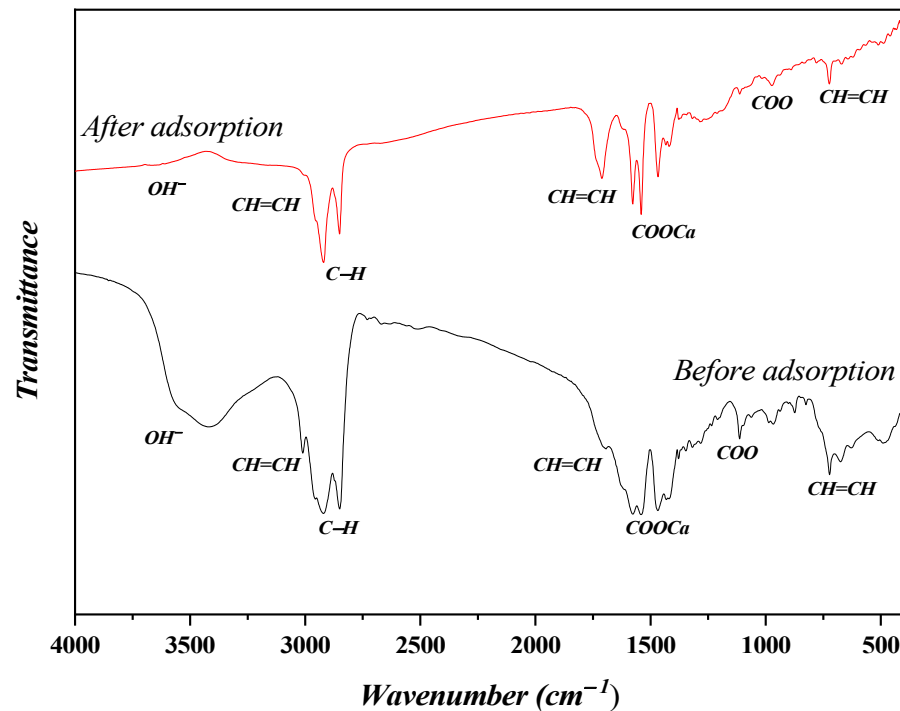


Figure 3. FTIR analysis performed on the adsorbent before and after the interaction with the MR dye.

The pH_{PZC} analysis enables finding the optimal pH for MR adsorption. Adsorption of anionic dyes is favored at pH values below the pH_{PZC} , while adsorption of cationic dyes is favored at pH values above the pH_{PZC} . Figure 4 presents the pH_{PZC} results for CaSF, showing that the difference between the initial pH and the final pH crosses the origin at $pH = 6$, which is the pH_{PZC} of CaSF. MR adsorption is favored when the pH of the medium is lower than the pH_{PZC} , as the CaSF surface is positively charged due to protonation. The ideal pH determined for the process was 4, as it is below CaSF's pH_{PZC} and provides for the electrostatic attraction between the positively charged CaSF surface and the negatively charged MR molecules. A pH of 4 was also considered optimal for the adsorption of MR on other adsorbents, such as activated carbon [1] and iron oxide nanoparticles [35].

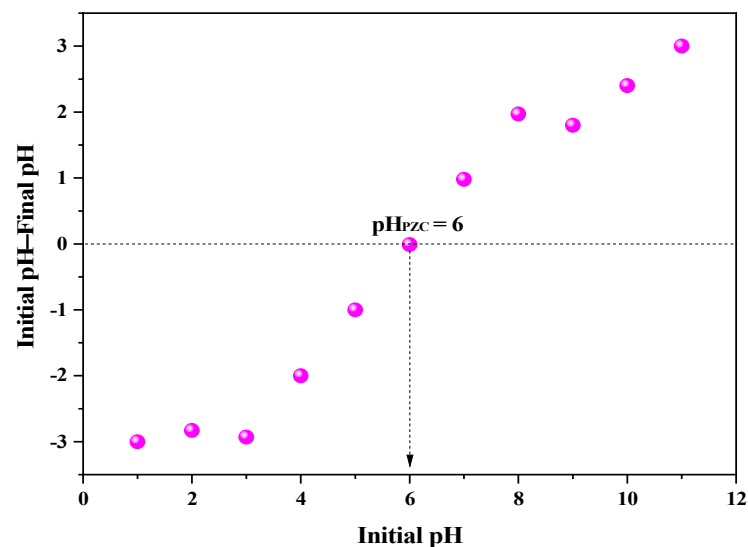


Figure 4. Relationship between initial and final pH to determine the pH_{PZC} .

3.2. CaSF Dosage

An adsorbent dosage analysis is essential to measure the amount of adsorbent necessary to attain the maximal MR removal efficiency. As shown in Figure 5, concentrations of CaSF below $2 \text{ g}\cdot\text{L}^{-1}$ are inefficient in removing MR molecules in the solution ($<1\%$). A CaSF dosage of $10 \text{ g}\cdot\text{L}^{-1}$ lead to the best MR removal, reaching a removal efficiency of 95.15%. Dosages above $10 \text{ g}\cdot\text{L}^{-1}$ did not show any significant increase in MR removal; therefore, it was considered the optimal dosage for the process. CaSF dosages of 1 and $2 \text{ g}\cdot\text{L}^{-1}$ were inefficient for removing MR, possibly due to the low number of active sites available to adsorb dye molecules and the consequent increased affinity to water of the MR molecules. The number of active sites available for adsorption was directly proportional to CaSF dosage, starting from $4 \text{ g}\cdot\text{L}^{-1}$. With an increase in dosage up to $10 \text{ g}\cdot\text{L}^{-1}$, the number of active sites and removal efficiency increased. Similar results have been found for the adsorption of MR by eggshell [20] and a metal–organic network [36].

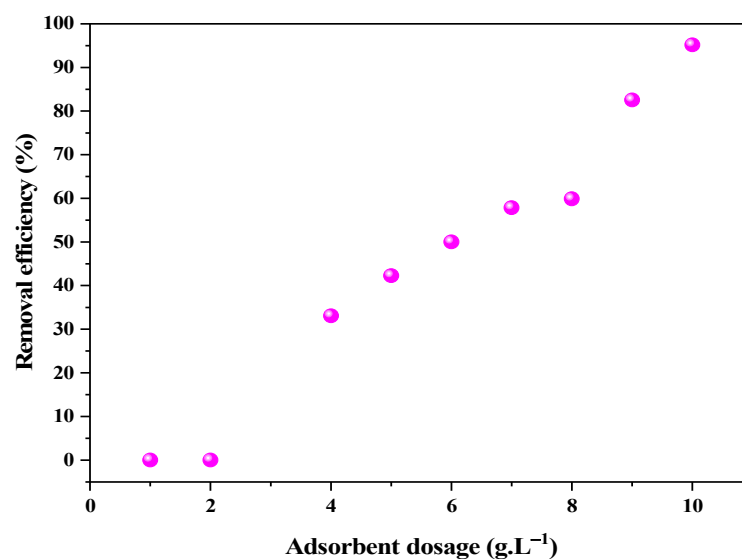


Figure 5. Relationship between MR removal efficiency and adsorbent amount, tested under a treatment of $10 \text{ mg}\cdot\text{L}^{-1}$ MR with $10 \text{ g}\cdot\text{L}^{-1}$ CaSF at $20 \text{ }^\circ\text{C}$, stirring the system at 100 rpm for 30 min .

3.3. Adsorption Kinetics

Kinetic adsorption models were used to study the mass transfer of free MR molecules in solution to the CaSF surface over time, as well as the time required for the process to reach a state of equilibrium. Figure 6 shows that the adsorption of MR occurs very quickly at the beginning of the treatment and then slows down until it reaches equilibrium after 30 min . The higher adsorption capacity in the first few minutes is the result of the high availability of free active sites on the CaSF surface. After the first 30 min , adsorption occurred with a low adsorption capacity due to the saturation of the CaSF active sites, in addition to the repulsive effect between the MR molecules already adsorbed on the CaSF and those free in the solution [37].

Tables 2 and 3 show that the kinetic model that best fits the experimental data was the PSO, with the highest R_{adj}^2 value ($R_{adj}^2 = 0.99$) and the lowest error values in the statistical analysis ($RSS = 0.01$; $X^2 = 7.78 \times 10^{-4}$; $AICc = -110.46$). Furthermore, this model retrieved the value of q_e closest to the adsorption capacity measured at experimental equilibrium (q_{e_exp}). The fact that the PSO model is the one that best fits the MR adsorption is a strong indication that chemisorption is the mechanism governing the process. Furthermore, it indicates that the adsorption rate is strongly dependent on MR concentration and on the availability of CaSF active sites. Similar results have been obtained using chitosan [18,38] and organosilicons [21].

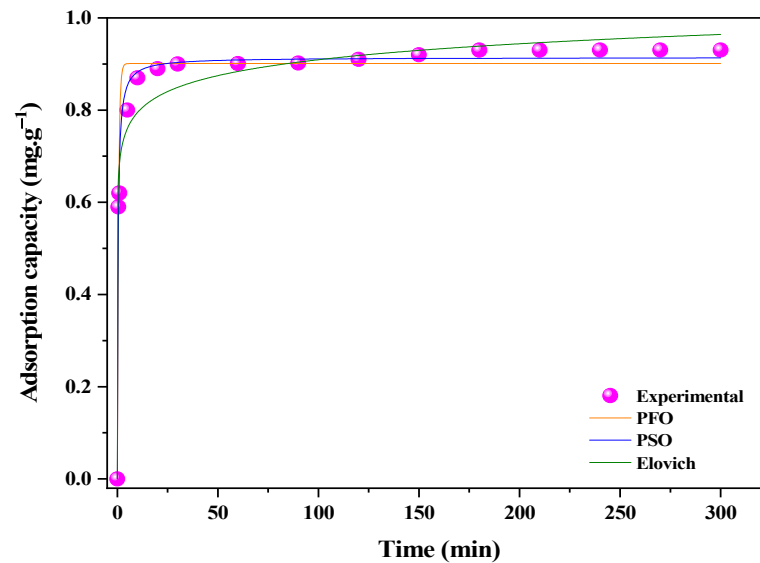


Figure 6. Experimental results and adsorption kinetics modeling for the treatment of $10 \text{ mg}\cdot\text{L}^{-1}$ MR with $10 \text{ g}\cdot\text{L}^{-1}$ CaSF at 20°C , stirring the system at 100 rpm.

Table 2. Adsorption kinetics parameters obtained for the treatment under optimized conditions.

Experimental Result	PFO		PSO		Elovich	
q_{e_exp} ($\text{mg}\cdot\text{g}^{-1}$)	q_e ($\text{mg}\cdot\text{g}^{-1}$)	k_1 (min^{-1})	q_e ($\text{mg}\cdot\text{g}^{-1}$)	k_2 ($\text{g}\cdot\text{mg}^{-1}\cdot\text{min}^{-1}$)	α ($\text{mg}\cdot\text{g}^{-1}\cdot\text{min}^{-1}$)	β ($\text{mg}\cdot\text{g}^{-1}$)
0.93	0.90	1.61	0.91	3.05	4.19×10^4	20.07

Table 3. Adsorption kinetics statistics obtained for the treatment under optimized conditions.

PFO				PSO				Elovich			
R_{adj}^2	RSS	X^2	AICc	R_{adj}^2	RSS	X^2	AICc	R_{adj}^2	RSS	X^2	AICc
0.96	0.03	2.47×10^{-3}	-92.90	0.99	0.01	7.78×10^{-4}	-110.46	0.97	0.02	1.67×10^{-3}	-99.18

3.4. Diffusion Mechanism

To understand the diffusion mechanism, the data were initially evaluated by the Weber–Morris adsorption model (intraparticle model). Figure 7 shows the formation of three different linear regions, representing different adsorption stages. Furthermore, the graph does not cross the origin, suggesting that intraparticle diffusion is not the only factor limiting the rate of MR adsorption. The first stage is attributed to a fast diffusion in the outer layer (film), the second is associated with intraparticle diffusion and the third represents the adsorption equilibrium [39]. Table 4 presents values of C that are not zero, indicating that the boundary layer influences the process. This finding corroborates the fact that intraparticle diffusion is not the only limiting step in the MR adsorption rate. The linear adjustment of the second stage showed a low R_{adj}^2 value, which could directly influence the value of K_d and generate complex and sometimes wrong interpretations of the adsorption mechanism.

Given the abovementioned limitation, the Boyd diffusion model (Figure 8) was applied in order to obtain more detailed information on the limiting step of MR adsorption on CaSF. The studied relationship does not cross the origin in the graph, indicating that the adsorption of MR on CaSF was mainly governed by a mass transfer in the outer layer (liquid film). Furthermore, the obtained value of D ($5.28 \times 10^{-9} \text{ cm}^2\cdot\text{s}^{-1}$) indicates a diffusional behavior with multiple controls, influenced by factors such as stirring rate, initial dye concentration, CaSF particle shape, number of pores in the adsorbent and

adsorption/desorption rate until the equilibrium state is reached. Figure 9 shows the adsorption mechanism suggested in this work. The free MR molecules in solution are believed to interact with the hydrophobic tails (covalent interactions) and hydrophilic heads (hydrogen bonds) of the CaSF surface.

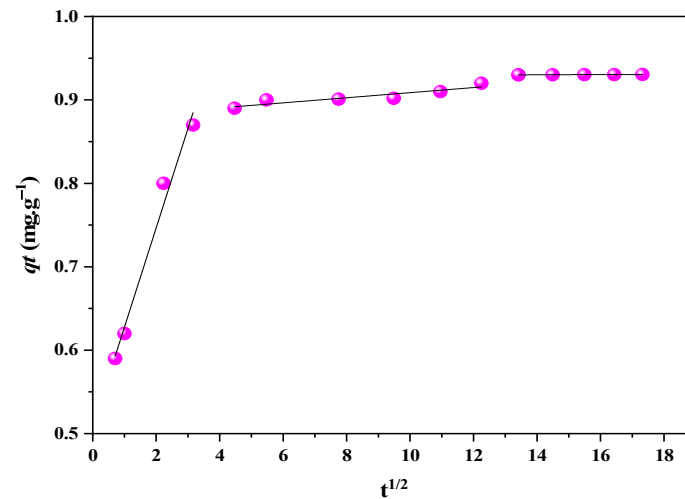


Figure 7. Weber–Morris diffusion model obtained for the treatment of 10 mg·L⁻¹ MR with 10 g·L⁻¹ CaSF at 20 °C, stirring the system at 100 rpm.

Table 4. Parameters of the Weber–Morris and Boyd diffusion models obtained under optimized conditions.

MR Conc. (mg·L ⁻¹)	q_{e_exp} (mg·g ⁻¹)	Weber–Morris				Boyd	
		Stage	C (mg·g ⁻¹)	K_d (mg·g ⁻¹ ·min ^{-0.5})	R_{adj}^2	RSS	D (cm ² ·s ⁻¹)
10	0.93	I	0.51	0.12	0.98	9.28×10^{-4}	5.28×10^{-9}
		II	0.88	3.06×10^{-3}	0.81	7.87×10^{-5}	
		III	0.93	1.02×10^{-4}	0.99	1.43×10^{-10}	

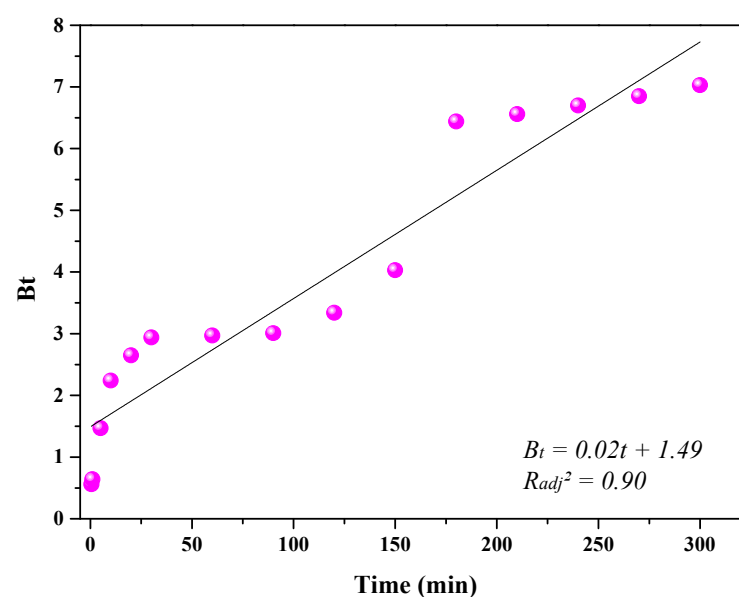


Figure 8. Boyd diffusion model observed for the treatment of 10 mg·L⁻¹ MR with 10 g·L⁻¹ CaSF at 20 °C, stirring the system at 100 rpm.

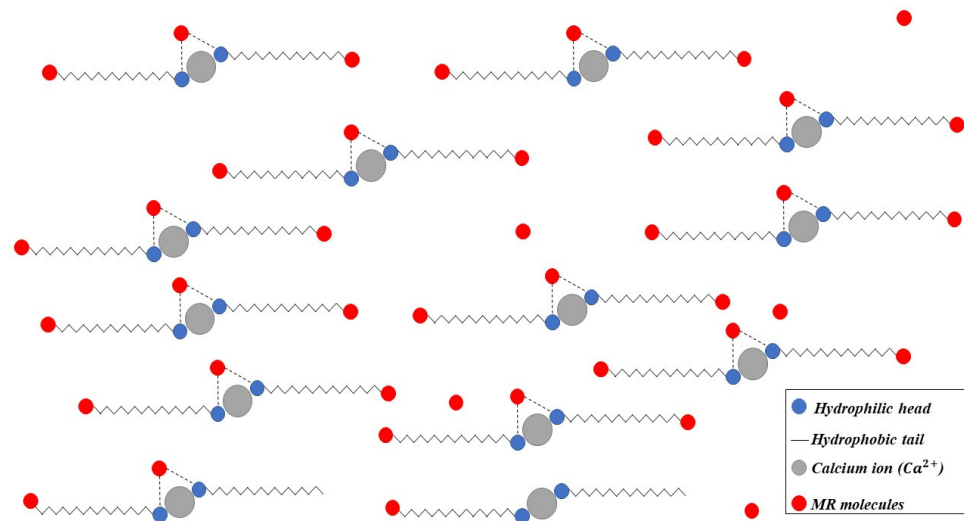


Figure 9. Proposed adsorption mechanism.

3.5. Adsorption Equilibrium

Adjusting the experimental data with the theoretical adsorption isotherm models makes it possible to estimate q_{max} for the CaSF dosage used, in addition to the type of adsorption taking place in the process (physical adsorption, chemisorption or both). Figure 10 shows the experimental data with the theoretical models at three different temperatures. The adsorption capacity of CaSF is extremely sensitive to temperature under all the dye concentrations studied. A temperature of 20 °C shows an increasing linear behavior with increasing MR concentrations, and does not reach a saturation stage (equilibrium). At 25 °C and 30 °C, however, saturation is reached for the last three tested concentrations, along with a sudden drop in CaSF adsorption capacity. This type of behavior can be attributed to the combination of the following factors: an exothermic MR adsorption process, pH range and CaSF's Krafft temperature.

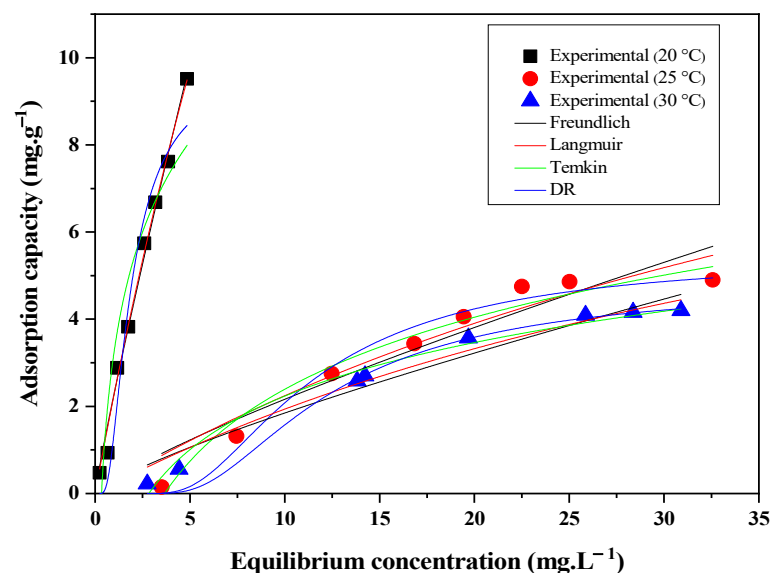


Figure 10. Adsorption isotherms observed for 10 g·L⁻¹ CaSF using different MR concentrations and stirring the system at 100 rpm for 30 min.

Regarding the nature of the process, Table 5 clearly shows the decrease both in the maximal experimental adsorption capacity (q_{max_exp}) and in the adsorption capacities calculated by the isotherm models (q_{max} and q_m), which indicate an exothermic process. In this

case, the increase in temperature promotes the agitation of the MR molecules, disfavoring their adsorption on the CaSF surface. The pH of the solution also influences the structure of CaSF, since it was synthesized from an anionic surfactant that undergoes deprotonation at pH values of <8 [40,41]. The data also showed evidence that an acidic pH can decrease the Krafft temperature of the CaSF, changing its stability, making it more soluble and hindering the adsorption of MR molecules. The increase in temperature reduces the efficiency of the process because the solubility of CaSF increases [42]. E values of > 16 kJ mol⁻¹ in the DR model indicated that dye adsorption occurred predominantly by chemisorption [32].

Table 5. Parameters of the isothermal adsorption models at different temperatures.

T (°C)	q_{max_exp} (mg·g ⁻¹)	Langmuir		DR		
		q_{max} (mg·g ⁻¹)	k_L (L·mg ⁻¹)	q_m (mg·g ⁻¹)	k_{DR} (mol ² ·kJ ⁻²)	E (kJ·mol ⁻¹)
20	9.52	53.59	0.04	9.73	7.82×10^{-7}	800
25	4.90	15.03	0.02	5.45	2.01×10^{-5}	158
30	4.20	11.69	0.02	4.80	2.30×10^{-5}	147
		Temkin		Freundlich		
		b (J·mol ⁻¹)	k_T (L·mg ⁻¹)	k_F (L·mg ⁻¹)		n
20	9.52	756.59	2.95	2.29		1.10
25	4.90	963.29	0.27	0.33		1.22
30	4.20	1.30×10^3	0.35	1.26		0.29

Table 6 presents the statistical analysis of the theoretical models using the experimental data. The best model is the one retrieving the highest value of R_{adj}^2 and the lowest values of X^2 , RSS and $AICc$. For a temperature of 20 °C, the Langmuir model had the best fit to the experimental data. Therefore, it is assumed that: (i) adsorption occurred with a formation of a monolayer, (ii) there is a defined number of sites with an equivalent energy, (iii) the adsorbed MR molecules do not interact with each other and (iv) each site can only hold one MR molecule [31]. However, the DR model fitted better to the experimental data at higher temperatures. Therefore, the adsorption of MR by CaSF occurred heterogeneously and with the formation of multilayers [43,44]. Table 7 compares the CaSF's q_{max} with those of other reported adsorbents for MR removal, proving that CaSF has an MR removal capacity similar or superior to those of other adsorbents already reported in the literature, showing its potential efficiency for the removal of MR from aquatic environments polluted with this dye.

Table 6. Statistical analysis of adsorption isotherm models at different temperatures.

T (°C)	Langmuir				DR				
	R_{adj}^2	RSS	X^2	$AICc$	R_{adj}^2	RSS	X^2	$AICc$	
20	0.99	0.51	0.08	-17.18	0.95	3.29	0.55	-2.31	
25	0.93	1.40	0.23	-9.20	0.98	0.44	0.07	-18.40	
30	0.97	0.48	0.08	-17.78	0.98	0.26	0.04	-22.59	
		Temkin			Freundlich				
		R_{adj}^2	RSS	X^2	$AICc$	R_{adj}^2	RSS	X^2	$AICc$
20		0.87	7.87	1.31	4.67	0.99	0.66	0.11	-15.34
25		0.97	0.63	0.10	-15.53	0.90	1.88	0.31	-6.80
30		0.98	0.34	0.06	-20.47	0.95	0.76	0.13	-14.02

Table 7. Comparison of MR adsorption capacities achieved by different adsorbents.

Adsorbent	Equilibrium (min)	pH	Temperature (°C)	q_{max} (mg·g ⁻¹)	Reference
Eggshell	180	2	25	1.66	20
Hydrogel	120	7	25	6.14	30
Sodium alginate	60	2	45	9.48	23
Chitosan	240	8	25	17.31	18
Organosilicons	3000	4.8	20	47.89	21
Coffee residues	240	3.5	25	66.66–76.72	45
Activated carbon	300	2	30	76.92	46
Activated carbon	50–80	4–5	30–50	435.25–226.90	1
Calcium surfactant	30	4	20	53.59	This study

The reuse of the material after adsorption has not yet been tested, but considering that is a nitrogen source, it could be used as a fertilizer. Another future goal is to study the regenerative capacity of the adsorbent, in order to improve the cost–benefit relationship for large-scale applications, in addition to using it as a precursor to synthesize carbon allotropes, to develop catalysts or as a template to produce nanoparticles.

4. Conclusions

Anionic surfactants can be used as adsorbents for the removal of azo dyes from aqueous matrices, as proven by the present study in which CaSF successfully removed 95.15% of the MR content. The achieved performance strongly depended on the controlled parameters, which included a pH of 4 and a CaSF dosage of 10 g·L⁻¹, which contribute to the greater availability of active sites for the capture of the azo dye molecules. Adsorption equilibrium was reached upon 30 min of treatment, and the PSO kinetic model was the one best fitting the experimental data. The adsorption mechanism was governed by mass transfer in the outermost layer due to hydrophobic interactions and hydrogen bonds established between the dye and the adsorbent. Temperature radically influenced the adsorption process and the increase in this variable hinders the efficiency of the process, a fact that points to its exothermic nature. As for the equilibrium conditions studied at 20 °C, the experimental data better fitted the Langmuir model ($q_{max} = 53.59 \text{ mg} \cdot \text{g}^{-1}$). However, when the process took place at higher temperatures, it was better defined by the DR model. Since the obtained adsorption capacity was equivalent to those observed with other natural and synthetic adsorbents, it can be stated that CaSF is a promising material for the removal of MR from matrices polluted with this azo dye. It should be noted that the use of CaSF as an adsorbent also has a sustainability aspect, as it can be produced from used frying oil, thus providing an adequate final destination for this waste, stimulating at the same time the circular economy.

Author Contributions: Conceptualization, Y.N.T., F.J.P.F. and T.M.B.F.O.; methodology, Y.N.T.; validation, Y.N.T., F.J.P.F. and T.M.B.F.O.; formal analysis, J.M.C.M., R.N.P.T., F.J.P.F. and T.M.B.F.O.; investigation, Y.N.T.; data curation, Y.N.T.; writing—original draft preparation, Y.N.T.; writing—review and editing, Y.N.T. and T.M.B.F.O.; visualization, F.J.P.F. and T.M.B.F.O.; supervision, F.J.P.F.; project administration, F.J.P.F. and T.M.B.F.O.; funding acquisition, F.J.P.F. and T.M.B.F.O. All authors have read and agreed to the published version of the manuscript.

Funding: The following Brazilian agencies supported this work: National Council for Scientific and Technological Development (CNPq; Proc. 420261/2018-4 and 308108/2020-5), Higher Education Personnel Improvement Coordination (CAPES; Finance code 001) and Cearense Foundation for Scientific and Technological Development Support (FUNCAP; Proc. BP3-0139-00276.01.00/18 and BP4-0172-00080.01.00/20).

Data Availability Statement: The data presented in this study are available within the manuscript.

Acknowledgments: All authors are grateful to the Federal University of Cariri (UFCA, Brazil) for encouraging and supporting the development of this work.

Conflicts of Interest: The authors declare that they have no known competing financial interests or personal relationships that could have appeared to influence the work reported in this paper.

References

1. Khan, E.A.; Shahjahan; Khan, T.A. Adsorption of methyl red on activated carbon derived from custard apple (*Annona squamosa*) fruit shell: Equilibrium isotherm and kinetic studies. *J. Mol. Liq.* **2018**, *249*, 1195–1211. [[CrossRef](#)]
2. Basu, S.; Ghosh, G.; Saha, S. Adsorption characteristics of phosphoric acid induced activation of bio-carbon: Equilibrium, kinetics, thermodynamics and batch adsorber design. *Process Saf. Environ. Prot.* **2018**, *117*, 125–142. [[CrossRef](#)]
3. Szygula, A.; Guibal, E.; Ruiz, M.; Sastre, A.M. The removal of sulphonated azo-dyes by coagulation with chitosan. *Colloid Surf. A Physicochem. Eng. Asp.* **2008**, *330*, 219–226. [[CrossRef](#)]
4. Zhang, L.; Gao, X.; Zhang, Z.; Zhang, M.; Cheng, Y.; Su, J. A doping lattice of aluminum and copper with accelerated electron transfer process and enhanced reductive degradation performance. *Sci. Rep.* **2016**, *6*, 31797. [[CrossRef](#)]
5. Greluk, M.; Hubicki, Z. Efficient removal of Acid Orange 7 dye from water using the strongly basic anion exchange resin Amberlite IRA-958. *Desalination* **2011**, *278*, 219–226. [[CrossRef](#)]
6. Martini, B.K.; Daniel, T.G.; Corazza, M.Z.; Carvalho, A.E. Methyl orange and tartrazine yellow adsorption on activated carbon prepared from boiler residue: Kinetics, isotherms, thermodynamics studies and material characterization. *J. Environ. Chem. Eng.* **2018**, *6*, 6669–6679. [[CrossRef](#)]
7. Pekov, G.; Petsev, N. Adsorption of methyl red on sterchamol. *Anal. Chim. Acta* **1990**, *232*, 413–416. [[CrossRef](#)]
8. Ashraf, S.S.; Rauf, M.A.; Alhadrami, S. Degradation of Methyl Red using Fenton's reagent and the effect of various salts. *Dye. Pig.* **2006**, *69*, 74–78. [[CrossRef](#)]
9. Cheng, X.H.; Guo, W. The oxidation kinetics of reduction intermediate product of methyl red with hydrogen peroxide. *Dye. Pig.* **2007**, *72*, 372–377. [[CrossRef](#)]
10. Muthuraman, G.; Teng, T.T. Extraction of methyl red from industrial wastewater using xylene as an extractant. *Prog. Nat. Sci.* **2009**, *19*, 1215–1220. [[CrossRef](#)]
11. Rios-Del Toro, E.E.; Celis, L.B.; Cervantes, F.J.; Rangel-Mendez, J.R. Enhanced microbial decolorization of methyl red with oxidized carbon fiber as redox mediator. *J. Hazard. Mater.* **2013**, *260*, 967–974. [[CrossRef](#)] [[PubMed](#)]
12. Sarkar, P.; Fakhruddin, A.N.M.; Pramanik, M.K.; Mahin, A.A. Decolorization of Methyl Red by *Staphylococcus arlettae* PF4 Isolated from Garden Soil. *Int. J. Environ.* **2011**, *1*, 34–39.
13. Ikram, M.; Naeem, M.; Zahoor, M.; Rahim, A.; Hanafiah, M.M.; Oyekanmi, A.A.; Shah, A.B.; Mahnashi, M.H.; Ali, A.A.; Jalal, N.A.; et al. Biodegradation of Azo Dye Methyl Red by *Pseudomonas aeruginosa*: Optimization of Process Conditions. *Int. J. Environ. Res. Public Health* **2022**, *19*, 9962. [[CrossRef](#)] [[PubMed](#)]
14. Sharifi, N.; Nasiri, A.; Martínez, S.S.; Amiri, A. Synthesis of Fe₃O₄@activated carbon to treat metronidazole effluents by adsorption and heterogeneous Fenton with effluent bioassay. *J. Photochem. Photobiol. A Chem.* **2022**, *427*, 113845. [[CrossRef](#)]
15. Tumlos, R.; Ting, J.; Osorio, E.; Rosario, L.; Ramos, H.; Ulano, A.; Lee, H.; Regalado, G. Results of the study of chemical-, vacuum drying- and plasma-pretreatment of coconut (*Cocos nucifera*) lumber sawdust for the adsorption of methyl red in water solution. *Surf. Coat. Technol.* **2011**, *205*, S435–S439. [[CrossRef](#)]
16. Ding, G.; Wang, B.; Chen, L.; Zhao, S. Simultaneous adsorption of methyl red and methylene blue onto biochar and an equilibrium modeling at high concentration. *Chemosphere* **2016**, *163*, 283–289. [[CrossRef](#)]
17. Luo, W.; Sasaki, K.; Hirajima, T. Influence of the pre-dispersion of montmorillonite on organic modification and the adsorption of perchlorate and methyl red anions. *Appl. Clay Sci.* **2018**, *154*, 1–9. [[CrossRef](#)]
18. Mozaffari, M.; Emami, M.R.S.; Binaeian, E. A novel thiosemicarbazide modified chitosan (TSFCS) for efficiency removal of Pb (II) and methyl red from aqueous solution. *Int. J. Biol. Macromol.* **2019**, *123*, 457–467. [[CrossRef](#)]
19. Zaheer, Z.; AL-Asfar, A.; Aazam, E.S. Adsorption of methyl red on biogenic Ag@Fe nanocomposite adsorbent: Isotherms, kinetics and mechanisms. *J. Mol. Liq.* **2019**, *283*, 287–298. [[CrossRef](#)]
20. Rajoriya, S.; Saharan, V.K.; Pundir, A.S.; Nigam, M.; Roy, K. Adsorption of methyl red dye from aqueous solution onto eggshell waste material: Kinetics, isotherms and thermodynamic studies. *Curr. Res. Green Sustain. Chem.* **2021**, *4*, 100180. [[CrossRef](#)]
21. Roik, N.V.; Belyakova, L.A.; Dziačko, M.O. Selective sorptive removal of Methyl Red from individual and binary component solutions by mesoporous organosilicas of MCM-41 type. *J. Environ. Sci.* **2021**, *99*, 59–71. [[CrossRef](#)] [[PubMed](#)]
22. Kim, H.; Purev, O.; Myung, E.; Choi, N.; Cho, K. Removal of methyl red from aqueous solution using polyethyleneimine crosslinked alginate beads with waste foundry dust as a magnetic material. *Int. J. Environ. Res. Public Health* **2022**, *19*, 9030. [[CrossRef](#)] [[PubMed](#)]
23. Adusei, J.K.; Agorku, E.S.; Voegborlo, R.B.; Ampong, F.K.; Danu, B.Y.; Amarh, F.A. Removal of methyl red in aqueous systems using synthesized NaAlg-g-CHIT/Nzvi adsorbent. *Sci. Afr.* **2022**, *17*, e01273. [[CrossRef](#)]
24. Weschayanwiwat, P.; Kunanupap, O.; Scamehorn, J.F. Benzene removal from wastewater using aqueous surfactant twophase extraction with cationic and anionic surfactant mixtures. *Chemosphere* **2008**, *72*, 1043–1048. [[CrossRef](#)]

25. Cavalcante, P.R.M.; Melo, R.P.F.; Castro Dantas, T.N.; Dantas Neto, A.A.; Barros Neto, E.L.; Moura, M.C.P.A. Removal of phenol from aqueous medium using micellar solubilization followed by ionic flocculation. *J. Environ. Chem. Eng.* **2018**, *6*, 2778–2784. [[CrossRef](#)]
26. Liu, H.Q.; Liu, F.; Wei, G.X.; Zhang, R.; Zhu, Y.W. Effects of Surfactants on the Removal of Carbonaceous Matter and Dioxins from Weathered Incineration Fly Ash. *Aerosol Air Qual. Res.* **2017**, *17*, 2338–2347. [[CrossRef](#)]
27. Hosseinzadeh, R.; Khorsandi, K.; Hemmaty, S. Study of the effect of surfactants on extraction and determination of polyphenolic compounds and antioxidant capacity of fruits extracts. *PLoS ONE* **2013**, *8*, e57353. [[CrossRef](#)]
28. Koner, S.; Pal, A.; Adak, A. Use of Surface Modified Silica gel factory Waste for Removal of 2,4-D Pesticide from Agricultural Wastewater: A case study. *Int. J. Environ. Res.* **2012**, *6*, 995–1006. [[CrossRef](#)]
29. Li, F.; Li, X.; Zhang, J.; Peng, L.; Liu, C. Removal of organic matter and heavy metals of low concentration from wastewater via micellar-enhanced ultrafiltration: An overview. *IOP Conf. Ser. Earth Environ. Sci.* **2017**, *52*, 012077. [[CrossRef](#)]
30. Fu, H.Y.; Zhang, Z.B.; Chai, T.; Huang, G.H.; Yu, S.J.; Liu, Z.; Gao, P.F. Study of the removal of aniline from wastewater via meuf using mixed surfactants. *Water* **2017**, *9*, 365. [[CrossRef](#)]
31. Lima, É.C.; Dehghani, M.H.; Guleria, A.; Sher, F.; Karri, R.R.; Dotto, G.L.; Tran, H.N. Adsorption: Fundamental Aspects and Applications of Adsorption for Effluent Treatment. In *Green Technologies for the Defluoridation of Water*; Elsevier: Amsterdam, The Netherlands, 2021; pp. 41–88.
32. Kaveeshwar, A.R.; Kumar, P.S.; Revellame, E.D.; Gang, D.D.; Zappi, M.E.; Subramaniam, R. Adsorption properties and mechanism of barium (II) and strontium (II) removal from fracking wastewater using pecan shell based activated carbon. *J. Clean. Prod.* **2018**, *193*, 1–13. [[CrossRef](#)]
33. Mirghani, M.E.S.; Che Man, Y.B.; Jinap, S.; Baharin, B.S.; Bakar, J. FTIR Spectroscopic Determination of Soap in Refined Vegetable Oils. *J. Am. Oil Chem. Soc.* **2002**, *79*, 111–116. [[CrossRef](#)]
34. Nandiyanto, A.B.D.; Oktiani, R.; Ragadhita, R. How to read and interpret FTIR spectroscopy of organic material. *Indones. J. Sci. Technol.* **2019**, *4*, 97–118. [[CrossRef](#)]
35. Dadfarnia, S.; Shabani, A.M.H.; Moradi, S.E.; Emami, S. Methyl red removal from water by iron based metal-organic frameworks loaded onto iron oxide nanoparticle adsorbent. *Appl. Surf. Sci.* **2015**, *330*, 85–93. [[CrossRef](#)]
36. Yılmaz, E.; Sert, E.; Atalay, F.S. Synthesis, characterization of a metal organic framework: MIL-53 (Fe) and adsorption mechanisms of methyl red onto MIL-53 (Fe). *J. Taiwan Inst. Chem. Eng.* **2016**, *65*, 323–330. [[CrossRef](#)]
37. Oyelude, E.O.; Awudza, J.A.M.; Twumasi, S.K. Removal of malachite green from aqueous solution using pulverized teak leaf litter: Equilibrium, kinetic and thermodynamic studies. *Chem. Cent. J.* **2018**, *12*, 81. [[CrossRef](#)]
38. Mohamed, H.G.; Aboud, A.A.; El-Salam, H.M.A. Synthesis and characterization of chitosan/polyacrylamide hydrogel grafted poly(N-methylaniline) for methyl red removal. *Int. J. Biol. Macromol.* **2021**, *187*, 240–250. [[CrossRef](#)]
39. Ngwabebhoh, F.A.; Erdem, A.; Yildiz, U. Synergistic removal of Cu(II) and nitrazine yellow dye using an eco-friendly chitosan-montmorillonite hydrogel: Optimization by response surface methodology. *J. Appl. Polym. Sci.* **2016**, *133*, 43664. [[CrossRef](#)]
40. Teixeira, Y.N.; Melo, R.P.F.; Fernandes, M.R.; Carmo, S.K.S.; Barros Neto, E.L. Malachite green removal using ionic flocculation. *Water Pract. Technol.* **2022**, *17*, 1113–1128. [[CrossRef](#)]
41. Teixeira, Y.N.; Paula Filho, F.J.; Bacurau, V.P.; Menezes, J.M.C.; Fan, A.Z.; Melo, R.P.F. Removal of Methylene Blue from a synthetic effluent by ionic flocculation. *Helyion* **2022**, *8*, e10868. [[CrossRef](#)] [[PubMed](#)]
42. Sultana, H.; Usman, M.; Ghaffar, A.; Bokhari, T.H.; Mansha, A.; Yusaf, A. Sustainable Application of Ionic Flocculation Method for Textile Effluent Treatment. In *Sustainable Practices in the Textile Industry*; Wiley: Hoboken, NJ, USA, 2021; pp. 253–272.
43. Ruthven, D.M. *Principles of Adsorption and Adsorption Process*, 1st ed.; John Wiley & Sons: Toronto, ON, Canada, 1984; p. 98.
44. Bonilla-Petriciolet, A.; Mendonza-Castillo, D.I.; Reynel-Ávila, H.E. *Adsorption Processes for Water Treatment and Purification*, 1st ed.; Springer: Cham, Switzerland, 2017; p. 33.

Disclaimer/Publisher’s Note: The statements, opinions and data contained in all publications are solely those of the individual author(s) and contributor(s) and not of MDPI and/or the editor(s). MDPI and/or the editor(s) disclaim responsibility for any injury to people or property resulting from any ideas, methods, instructions or products referred to in the content.